



CHORUS

This is the accepted manuscript made available via CHORUS. The article has been published as:

Interatomic Potential in the Nonequilibrium Warm Dense Matter Regime

Z. Chen, M. Mo, L. Souldard, V. Recoules, P. Hering, Y.Y. Tsui, S. H. Glenzer, and A. Ng
Phys. Rev. Lett. **121**, 075002 — Published 15 August 2018

DOI: [10.1103/PhysRevLett.121.075002](https://doi.org/10.1103/PhysRevLett.121.075002)

Interatomic potential in the non-equilibrium warm dense matter regime*

Z. Chen¹, M. Mo¹, L. Souillard², V. Recoules², P. Hering¹, Y.Y. Tsui³, S.H. Glenzer^{1,†}, and A. Ng^{4,*}

¹*SLAC National Accelerator Laboratory, Menlo Park, California, U.S.A.*

²*CEA, DAM, DIF, 91297 Arpajon, France*

³*Department of Electrical and Computer Engineering,
University of Alberta, Edmonton, Alberta, Canada*

⁴*Department of Physics and Astronomy, University of British Columbia, Vancouver, British Columbia, Canada*

(Dated: July 22, 2018)

We present a new measurement of lattice disassembly times in *f*s-laser heated polycrystalline Au nanofoils. The results are compared with molecular dynamics simulations incorporating a highly optimized, embedded-atom-method interatomic potential. For absorbed energy densities of 0.9-4.3MJ/kg, the agreement between experiment and simulation reveals a single-crystal like behavior of homogeneous melting and corroborates the applicability of the interatomic potential in the non-equilibrium warm dense matter regime. For energy densities below 0.9MJ/kg, the measurement is consistent with nanocrystal behavior where melting is initiated at the grain boundaries.

PACS numbers: 52.50.Jm, 52.27.Gr, 71.15.-m, 72.80.-r

The understanding of the properties of matter depends on an accurate knowledge of its electronic and ionic structures. For the calculation of electronic structure, density functional theory (DFT) is the most widely used method whereas for the ionic structure, molecular dynamics (MD) simulation plays a parallel role. Central to MD simulation are the interatomic forces. While first principles approaches can provide accurate derivation of interatomic forces, they are intractable for large-scale simulations particularly for metals. Such approaches are generally limited to calculations for small systems and short times. The alternative approach is to treat interatomic interactions via an interatomic potential. Different many-body potentials have been proposed. Popular among them is the embedded-atom-method (EAM) potential that is rooted in DFT [1]. Its mathematic simplicity also renders it conducive to large-scale simulations. Traditionally, the potential is parameterized and fitted to a limited number of known physical properties [2–5]. This may be inadequate for describing states outside the range of the fitting parameters. Alternatively, interatomic potentials have been developed by fitting the potential energy surface (PES) derived from first principles calculations, with or without the use of experimental data [6–13]. However, the single PES used described the ground state only. This excludes electronic effects of excited states such as phonon hardening [14]. A challenging new question is the applicability of such interatomic potentials in the non-equilibrium warm dense matter regime that is characterized by degenerate and excited electrons as well as strongly correlated ions. This issue is particularly timely driven by the proliferation of experimental studies of such states produced by intense, ultrafast lasers [15–23], FEL [24–29], and laser-driven ion sources [30–35], together with the interest to model their behaviors and properties using MD simulations [22, 23, 36–42]. Here we report on the first assessment of such applicability by

comparing MD simulations with the measurement of lattice disassembly times in *f*s-laser heated Au nanofoils at an energy density up to 4.3MJ/kg.

In our experiment, a 400nm, 45fs (FWHM) laser beam is focused to a $99\pm 3\mu\text{m}$ -diameter (FWHM) Gaussian spot at normal incidence on a freestanding, 30nm-thick, polycrystalline Au foil with a maximum intensity of $1.1\times 10^{13}\text{W}/\text{cm}^2$. The absorbed laser energy is determined from simultaneous measurements of the incident, reflected and transmitted pump pulse with $5\mu\text{m}$ spatial resolution. Laser absorption occurs by skin-depth deposition, dominated by the excitation of *5d* electrons to the conduction band. This is followed by ballistic electron transport and reflux inside the foil, producing uniform energy density in $\sim 100\text{fs}$ [20]. To determine the disassembly of the heated foil, the motion of the front and rear surfaces of the foil is monitored by Frequency Domain Interferometry (FDI) [16, 43]. This diagnostic measures the change in phase shift, $\Delta\phi$, of a specular reflected probe laser beam. The value of $\Delta\phi$ is governed by both the ac conductivity of the foil and the velocity of its free surface when expansion occurs. The S-polarized probe beam is incident onto the foil at 12° with a spot diameter of $500\mu\text{m}$ (FWHM). The spatial resolution of the diagnostic is $11\mu\text{m}$. A vital feature of the current FDI diagnostic is the use of a frequency-chirped 800nm, $\sim 15\text{ps}$ (FWHM) probe pulse to allow the measurement of temporal evolution in segments of $\sim 15\text{ps}$ each. This improves significantly the fidelity in recording temporal changes in each segment. The same advantage also extends to measurements using multiple segments to probe temporal changes over longer durations. The resolution of the temporal record is $\sim 800\text{fs}$, with sensitivity to surface motion of $\sim 1\text{nm}$. In comparison, earlier study of lattice disassembly [16] was made using an 800nm, 145fs(FWHM) probe laser. The temporal evolution of the phase shift at each absorbed energy density was obtained by scanning

the pump-probe delays at small intervals, using a total of over 100 shots. The precision of the measured disassembly time was severely limited by shot-to-shot variations in the pump laser intensity. Further discussion can be found in the Supplemental Material and references therein [44–49].

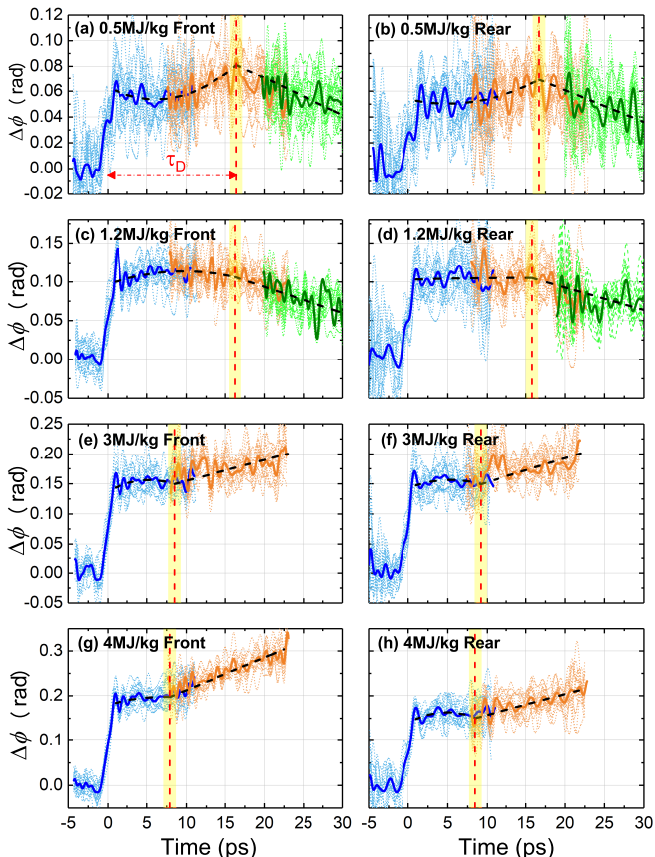


FIG. 1. Temporal changes in phase shifts. Time zero marks the pump laser pulse peak. The data for different temporal segments are displayed with different color traces. The thin traces are results from individual shots and the thick traces are their corresponding values averaged over 10-15 shots. The black dashed line marks the onset of disassembly with the uncertainty marked by the yellow band.

Samples of the new FDI data are presented in Fig. 1. The initial rise in $\Delta\phi$, varying from 0.06 to 0.2 rad, is caused by laser-induced changes in ac conductivity of the heated foil. The small overshoot results from interference [50] caused by cross phase modulation and spectral broadening [51] due to pump-induced optical Kerr effect [52], as seen in earlier experiments [20, 21]. Fig. 2 shows the dependence of the initial $\Delta\phi$ on absorbed energy density $\Delta\varepsilon$. Also displayed are the corresponding values calculated from the ac conductivity measured at the same laser heating conditions [21]. The good agreement validates the FDI measurement and the absence of significant foil expansion at this early time.

The subsequent evolution of $\Delta\phi$ is a complex interplay

of competing processes. Initially, thermal expansion of the lattice can lead to an increase in $\Delta\phi$ due to surface motion and at the same time a reduction of $\Delta\phi$ due to the decrease in electron density. Further discussion can be found in the Supplemental Material and references therein [44, 53–57]. When the lattice expansion waves meet at the center of the foil (4.2ps), a tensile zone appears. The subsequent reflections of these waves at the free surface leads to a succession of compression and tensile waves. The variation of $\Delta\phi$ associated with these waves appears to be small and the effect is visible only at low energy density (Figs. 1a-1d). This process is interrupted when the foil disassembles. The resulting release of the molten state by a rarefaction wave propagating into the foil produces a plasma plume comprising an electron density gradient ∇n_e and an accompanying ac conductivity gradient $\nabla\sigma$. These gradients are governed respectively by hydrodynamics and the dependence of σ on n_e . Calculations of electromagnetic wave propagation through the nanofoil show that $\Delta\phi$ increases with time when the $\nabla\sigma$ tracks ∇n_e but decreases when $\nabla\sigma$ become much steeper than ∇n_e . The possibility of such different temporal behaviors in $\Delta\phi$ is consistent with earlier observations [16] and the current measurement. To determine the onset of disassembly in Fig. 1, the slowly varying segment of $\Delta\phi$ after the initial jump (response to laser heating) is fitted to a quadratic function while the following rapidly changing segment is fitted to a linear function, as guided by the apparent temporal trends exhibited by the data in the absence of available theoretical predictions. The crossover point is chosen to produce the minimum least square error in the fitting of the two functions. This then marks the onset of disassembly as indicated by the vertical red dash line (Fig. 1). A yellow band is included to show the associated uncertainty.

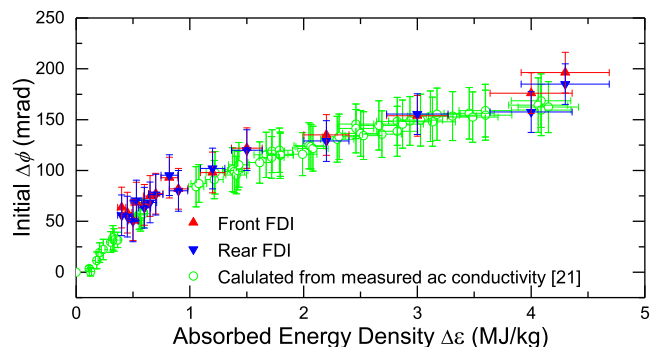


FIG. 2. Initial change in phase shift as a function of absorbed energy density.

Fig. 3 shows the dependence of the foil disassembly time on $\Delta\varepsilon$. The data reveals two different regimes of behavior, with the disassembly time showing a different scaling with absorbed energy density above and below 0.9MJ/kg. Also shown are results from [16], which could

not resolve the transition between these two regimes.

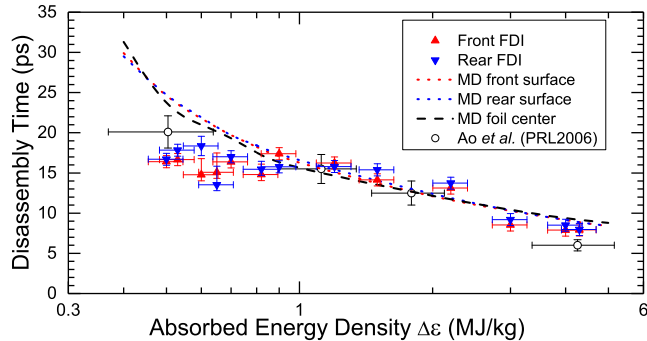


FIG. 3. Foil disassembly time as a function of $\Delta\phi$. Time zero marks the pump laser pulse peak. Note that in the Ao *et al.* data [16], disassembly time is measured from the end of the pump pulse 150fs after its peak.

To understand these macroscopic observations, we have performed Two-Temperature Molecular Dynamics (2T-MD) simulations with the STAMP code developed at CEA, for our experimental conditions using a similar approach described by Ivanov and Zhigilei [36, 37] except for two crucial changes. First, the free-electron-gas electron specific heat $C_e(T_e)$ is replaced by the one derived from a T_e -dependent electron density of states obtained from DFT calculations [49]. The validity of this $C_e(T_e)$ has been demonstrated in the measurement of ac conductivity of warm dense Au at energy densities up to 4.5MJ/kg [21]. Second, for interatomic potential we have chosen the highly optimized EAM potential developed recently by Sheng *et al.* [13]. For each of the fourteen face-centered-cubic elements described, several hundred atomic configurations are used in high-precision *ab initio* calculations to form the PES. The latter is combined with accurate experimental data on elastic constants and phonon frequencies to optimize the potential. Pertinent to our study is the potential for Au that has yielded agreement with experiment over a broader range of physical properties than other potentials [58–60] in equilibrium condition. Specifically, it yields a melting point of 1320K, melting enthalpy of 11.1kJ/mol and a liquid density at 1500K of 17.1g/cm³, compared with corresponding experimental values of 1337K, 12.8kJ/mol and 17.1g/cm³. However, the potential has yet to be tested in the warm dense matter regime.

In the MD simulations by Ivanov and Zhigilei [36, 37], the electron-ion coupling factor g_{ei} is set to a constant value of $2.1 \times 10^{16} \text{W/m}^3\text{K}$, taken from the measurement of Au at low energy densities by Hohlfeld *et al.* [47]. A T_e -dependent g_{ei} can also be calculated. A well-known approach is the description of electron-phonon energy exchange for arbitrary electron density of states developed by Allen [61] based on the rate equation for electron-phonon-collisions [49, 62]. In contrary, Dharma-wardana and Perrot [63] have advocated that electron and ion den-

sity fluctuations in warm dense matter should be treated as a coupled mode. This leads to significantly weaker electron-ion coupling. A similar finding has also been reported by Vorberger *et al.* [64]. Furthermore, in a recent study of Au under similar conditions [21] the observed temporal evolution of ac conductivity for energy densities from 0.55-4MJ/kg is found to be consistent with the g_{ei} obtained by Hohlfeld *et al.* [47]. Accordingly, we have retained $g_{ei}=2.1 \times 10^{16} \text{W/m}^3\text{K}$ in our 2T-MD simulations.

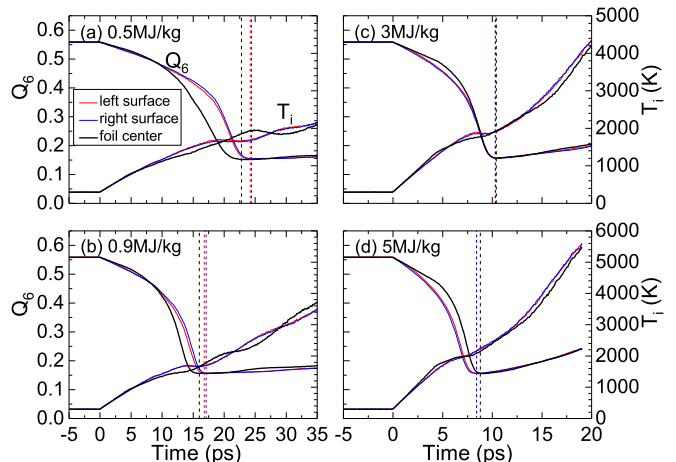


FIG. 4. Temporal evolution of the order parameter Q_6 and ion temperature T_i : Time zero marks the pump laser pulse peak. The vertical dashed lines identify the time for minimum Q_6 .

The initial geometry of our MD simulation is a parallelepiped with $73 \times 100 \times 100$ unit cells (2,920,000 atoms). The boundaries are periodic along the y and z axes, and free along the x-axis that aligns with the thickness of the Au foil.

In the simulation, the lattice structure including the solid-liquid transition is governed by the interatomic potential while the time scale for the change in lattice structure is regulated by g_{ei} . To quantify the change in lattice structure of Au, we have chosen the bond-orientational order parameter Q_6 [65] that exhibits the greatest change with melting, decreasing from 0.56 at ambient conditions to the minimum value of 0.155 when fully molten. The temporal evolution of Q_6 at the free surfaces and foil center is presented in Fig. 4. The rate of disorder is similar at the surface and the center of the foil, with an initial decrease of Q_6 to 0.4 due to lattice vibrations followed by a much more rapid reduction as the lattice melts. Complete melting ensues when Q_6 reaches a minimum value. This occurs almost simultaneously at foil center and the surfaces. The time difference is limited to 2ps even at an energy density of 0.5MJ/kg, where melting occurs first at the foil center. This behavior is indicative of homogeneous melting under ultrafast heating conditions that is predicted in earlier simulations [36, 37]. Fig. 4 also

shows the correlation of the change in ion temperature with melting.

The times needed to reach complete melting at the foil center and the free surfaces are compared with the measured disassembly time (Fig. 3). For $\Delta\epsilon > 0.9\text{MJ/kg}$, the agreement indicates that the *fs*-laser heated polycrystalline Au nanofoil approaches the behavior of a single crystal with melting occurring in a homogenous process under superheating conditions. Such a behavior at high energy density has been found in MD simulations of nanocrystalline Au foils [42]. Our result thus yields the first corroboration of the applicability of the highly optimized EAM potential of Sheng *et al.* [13] in the warm dense matter regime. Above 0.9MJ/kg , our two-temperature model shows an ion heating rate exceeding $6.3 \times 10^{13}\text{K/s}$ when T_i reaches the normal melting point of 1337K . Furthermore, the effect of T_e on interatomic potential appears to remain insignificant up to 4.3MJ/kg . This may be the result of competing processes. While the increase in T_e may lead to phonon hardening and rise in the melting temperature under constant density conditions [14], the change in interatomic potential with elevated electron temperature may also cause increase in lattice expansion that leads to phonon softening [22].

For $\Delta\epsilon < 0.9\text{MJ/kg}$ (Fig. 3), the observed disassembly times of the polycrystalline Au foils become much shorter than the melting time predicted from our MD simulation for single crystal Au foils. This is attributed to the decrease in ion heating rate below $6.3 \times 10^{13}\text{K/s}$, allowing melting to be initiated at the grain boundaries near the normal melting temperature. The melting process is accelerated by the propagation of the melt front towards the center of the nanocrystal. Such a behavior at low energy density is consistent with MD simulations of nanocrystalline Au foils [42]. The speed of the melt front is kinetically limited to several percent of the sound speed at room temperature.

In addition to the validation of interatomic potential, our simulations also provide further insight into the complex role of compression and tensile waves on melting in *fs*-laser heated nanofoils. Fig. 5 shows the temporal history of pressure and density at foil center $\Delta\epsilon > 0.9\text{MJ/kg}$. Prior to the arrival of the lattice expansion wave at $\sim 4.6\text{ps}$, pressure increases along an isochore. This is followed by the decrease in pressure and density in a tensile wave. The reflection of the tensile wave from the free surfaces leads to recompression, followed by a second tensile wave where melting is completed. Throughout this process, T_i continues to increase driven by electron-ion coupling (Fig. 4). The evolution of pressure, density and T_i at foil center as it changes from a cold solid with $T_i = 300\text{K}$ to a completely molten state is displayed in Figs. 6(a) and 6(b). Figs. 6(c) and 6(d) show the loci of the resulting molten states in the phase diagrams for energy densities between 0.9 to 5MJ/kg . This suggests that while the condition for melting is dictated by

the interatomic potential, the molten state reached is determined by the propagation of compression and tensile waves in the nanofoil.

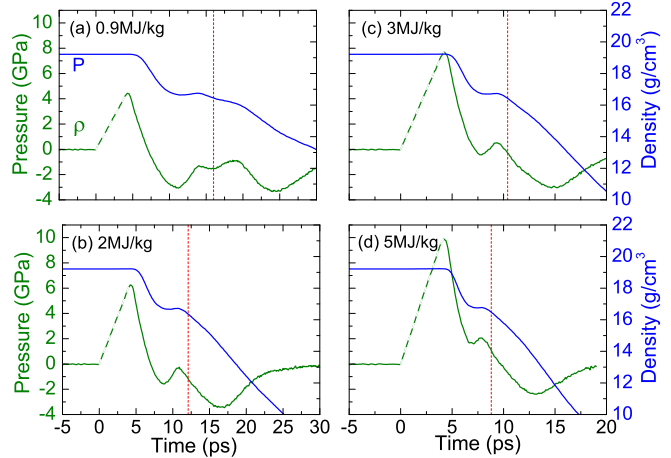


FIG. 5. Temporal evolution of pressure and density at foil center. Time zero marks the pump laser pulse peak. The green dashed line is an isochore.

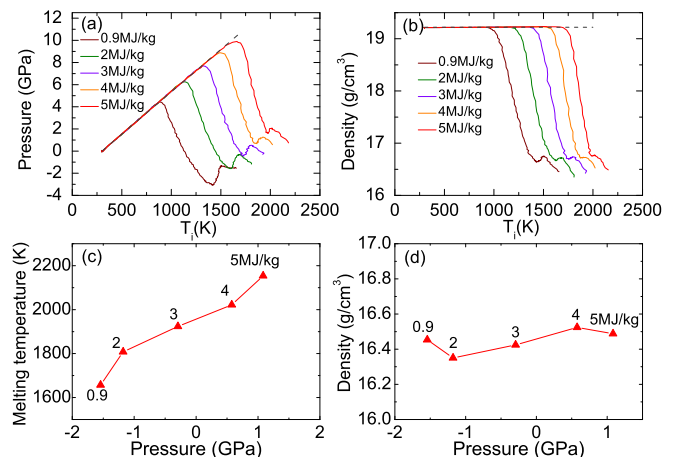


FIG. 6. Evolution of pressure, density and ion temperature in foil center as it changes from a cold solid to a completely molten state. The black dashed line is the isochore.

In conclusion, our measured lattice disassembly times in *fs*-laser heated polycrystalline Au nanofoils with $\Delta\epsilon$ of 0.9 - 4.3MJ/kg show good agreement with the results of Two-Temperature Molecular Dynamics simulations based on a highly optimized embedded-atom-method interatomic potential [13]. This indicates that the polycrystalline nanofoils approaches the behavior of single-crystal nanofoils with melting occurring in a homogenous process under superheating conditions. Equally importantly, it corroborates the applicability of the embedded-atom-method potential in the non-equilibrium warm dense matter regime. As illustrated in the Two-Temperature Molecular Dynamics simulations, the compression and

tensile waves initiated by lattice expansion play a significant role in the melting of nanofoils. This underscores the need to understand the dynamic changes of warm dense matter states produced in nanofoils for the proper interpretation of experiments. For energy densities below 0.9MJ/kg, our result suggests that melting is initiated at the grain boundaries where the ion heating rate becomes less than 6.3×10^{13} K/s when T_i reaches 1337K. Melting becomes dominated by the polycrystalline structure of the nanofoil. Furthermore, the observed single-crystal-like melting behavior at high energy density and the poly-crystal melting behavior at low energy density also corroborate the Molecular Dynamics simulation of nanocrystalline Au nanofoils [42].

This study was supported by DOE Office of Science, Fusion Energy Science under FWP 100182, SLAC National Accelerator Laboratory Directed Research and Development Program, and Natural Sciences and Engineering Research Council of Canada.

* nga@physics.ubc.ca; † glenzer@slac.stanford.edu

- [1] M.S. Daw and M.I. Baskes, Phys. Rev. Lett. **50**, 1285 (1983).
- [2] M.S. Daw and M.I. Baskes, Phys. Rev. B **29**, 6443 (1984).
- [3] S.M. Foiles, M.I. Baskes, and M.S. Daw, Phys. Rev. B **33**, 7983 (1986).
- [4] R. A. Johnson, Phys. Rev. B **39**, 12554 (1989).
- [5] Y. Mishin, D. Farkas, M.J. Mehl, and D.A. Papaconstantopoulos, Phys. Rev. B **59**, 3393 (1999).
- [6] T.J. Lenosky *et al.*, Simul. Mater. Sci. Eng. **8**, 825 (2000).
- [7] A.T. van Duijn, S. Dasgupta, F. Lorant, and W.A. Goddard III, J. Phys. Chem. A **105**, 9396 (2001).
- [8] J.D. Gale and A.L. Phoh, Mol. Simul. **29**, 291 (2003).
- [9] P. Brommer and F. Gahler, Modell. Simul. Mater. Sci. Eng. **15**, 295 (2007).
- [10] J. Behler and M. Parrinello, Phys. Rev. Lett. **98**, 146401 (2007).
- [11] Y. Q. Cheng, E. Ma, and H.W. Sheng, Phys. Rev. Lett. **102**, 245501 (2009).
- [12] M.R. Fellingner, H. Park, and J.W. Wilkins, Phys. Rev. B **81**, 144119 (2010).
- [13] H.W. Sheng, M.J. Kramer, A. Cadien, T. Fujita, and M.W. Chen, Phys. Rev. B **83**, 134118 (2011).
- [14] V. Recoules, J. Clerouin, G. Zerah, P.M. Anglade, and S. Mazevet, Phys. Rev. Lett. **96**, 055503 (2006).
- [15] K. Widmann *et al.*, Phys. Rev. Lett. **92**, 125002 (2004).
- [16] T. Ao *et al.*, Phys. Rev. Lett. **96**, 055001 (2006).
- [17] Y. Ping *et al.*, Phys. Rev. Lett. **96**, 255003 (2006).
- [18] R. Ernstorfer *et al.*, Science **323**, 1033 (2009).
- [19] B.I. Cho *et al.*, Phys. Rev. Lett. **106**, 167601 (2011).
- [20] Z. Chen *et al.*, Phys. Rev. Lett. **108**, 165001 (2012).
- [21] Z. Chen *et al.*, Phys. Rev. Lett. **110**, 135001 (2013).
- [22] A.L. Daraszewicz *et al.*, Phys. Rev. B **88**, 184101 (2013).
- [23] Y. Giret *et al.*, Appl. Phys. Lett. **103**, 203107 (2013).
- [24] B. Nagler *et al.*, Nature Phys. **5**, 693 (2009).
- [25] S.P. Hau-Riege *et al.*, Phys. Rev. Lett. **108**, 217402 (2012).
- [26] A. Levy *et al.*, Phys. Plasmas **22**, 030703 (2015).
- [27] U. Zastra *et al.*, Phys. Rev. Lett. **112**, 105002 (2014).
- [28] P. Sperling *et al.*, Phys. Rev. Lett. **115**, 115001 (2015).
- [29] B.B.L. Witte *et al.*, Phys. Rev. Lett. **118**, 225001 (2017).
- [30] P.K. Patel *et al.*, Phys. Rev. Lett. **91**, 125004 (2003).
- [31] G.M. Dyer *et al.*, Phys. Rev. Lett. **101**, 015002 (2008).
- [32] T.G. White *et al.*, Sci. Reports **2**, 889 (2012).
- [33] D.J. Hoarty *et al.*, High Energy Density Physics **8**, 50 (2012).
- [34] W. Bang *et al.*, Sci. Rep. **5**, 14318 (2015).
- [35] W. Bang *et al.*, Phys. Rev. E **92**, 063101 (2015).
- [36] D.S. Ivanov and L.V. Zhigilei, Phys. Rev. Lett. **91**, 105701 (2003).
- [37] D.S. Ivanov and L.V. Zhigilei, Phys. Rev. B **68**, 064114 (2003).
- [38] S. Mazevet *et al.*, Phys. Rev. Lett. **95**, 085002 (2005).
- [39] Z. Lin and L.V. Zhigilei, Phys. Rev. B **73**, 184113 (2006).
- [40] D.S. Ivanov and L.V. Zhigilei, Phys. Rev. Lett. **98**, 195701 (2007).
- [41] Z. Lin and L.V. Zhigilei, J. Phys.: Conf. Ser. **59**, 11 (2007).
- [42] Z. Lin, E. Leveugle, M. Bringa, and L.V. Zhigilei, J. Phys. Chem. C **114**, 5686 (2010).
- [43] J.P. Geindre *et al.*, Opt. Lett. **19**, 1997 (1994).
- [44] Supplemental Material [url:]
- [45] T. Ao, Ph.D Thesis, University of British Columbia (2006).
- [46] J. Hohlfeld, J.G. Muller, S.-S. Wellershoff, and E. Matthisa, Appl. Phys. B **64**, 387 (1997).
- [47] J. Hohlfeld, S.-S. Wellershoff, J. Gudde, *et al.*, Chem. Phys. **251**, 237 (2000).
- [48] Yu.V. Petrov, N.A. Inogamov, and K.P. Migdal, JETP Lett. **97**, 24 (2013).
- [49] B. Holst, V. Recoules, S. Mazevet, *et al.*, Phys. Rev. B **90**, 035121 (2014).
- [50] E. Tokunaga, A. Terasakiy, and T. Kobayashi, J. Opt. Soc. Am. B **12**, 753 (1995).
- [51] K.Y. Kim, I. Alexeev, and H.M. Milchberg, Appl. Phys. Lett. **81**, 1424 (2002).
- [52] F. Hache, D. Ricard, C. Flytzanis, and U. Kreibig, Appl. Phys. A **47**, 347 (1988).
- [53] A. Ng, P. Sterne, S. Hansen, *et al.*, Phys. Rev. E **94**, 033213 (2016).
- [54] U. Samir, K.H. Wright, Jr. and N.H. Stone, Rev. Geophys. & Space Physics **21**, 1631 (1983).
- [55] A. Forsman, A. Ng, G. Chiu, and R.M. More, Phys. Rev. E **58**, R1248
- [56] A.W. DeSilva and J.D. Katsouros, Phys. Rev. E **57**, 5945 (1998).
- [57] M. Born and E. Wolf, *Principles of Optics, 6th ed.*, Pergamon Press, Oxford, 1980.
- [58] F. Ercolessi, M. Parrinello, and E. Tosatti, Philos. Mag. A **58**, 213 (1988).
- [59] B.J. Lee, J.H. Shim, and M.I. Bakes, Phys. Rev. B **68**, 144112 (2003).
- [60] G. Grochola, S.P. Russo, and I.K. Snook, J. Chem. Phys. **134**, 204719 (2005).
- [61] P.B. Allen, Phys. Rev. Lett. **59**, 1460 (1987).
- [62] Z. Lin and L.V. Zhigilei, Phys. Rev. B **77**, 075133 (2008).
- [63] M.W.C. Dharma-wardana and F. Perrot Phys. Rev. E **58** 3705 (1998).
- [64] J. Vorberger *et al.*, Phys. Rev. E **81** 046404 (2010).
- [65] P.J. Steinhardt, D.R. Nelson, and M. Ronchetti, Phys. Rev. B **28** 784 (1983).